RAA 2020 Vol. **20** No. **12**, 195(14pp) doi: 10.1088/1674-4527/20/12/195

http://www.raa-journal.org *http://iopscience.iop.org/raa*

***R**esearch in*
***A**stronomy and*
***A**strophysics*

The intrinsic SFRF and sSFRF of galaxies: comparing SDSS observation with IllustrisTNG simulation

Ping Zhao[1], Haojie Xu[1], Antonios Katsianis[2,1] and Xiao-Hu Yang[1,2]

[1] Department of Astronomy, School of Physics and Astronomy, Shanghai Jiao Tong University, Shanghai 200240, China
[2] Tsung-Dao Lee Institute, and Shanghai Key Laboratory for Particle Physics and Cosmology, Shanghai Jiao Tong University, Shanghai 200240, China; *haojie.xu@sjtu.edu.cn, kata@sjtu.edu.cn*

Received 2020 April 5; accepted 2020 May 30

Abstract The star formation rate function (SFRF) and specific star formation rate function (sSFRF) from observations are impacted by the Eddington bias, due to uncertainties in the estimated star formation rate (SFR). We develop a novel method to correct the Eddington bias and obtain the intrinsic SFRF and sSFRF from the Sloan Digital Sky Survey (SDSS) Data Release 7. The intrinsic SFRF is in good agreement with measurements from previous data in the literature that relied on UV SFRs but its high star-forming end is slightly lower than the corresponding IR and radio tracers. We demonstrate that the intrinsic sSFRF from SDSS has a bimodal form with one peak found at $\mathrm{sSFR} \sim 10^{-9.7}\ \mathrm{yr}^{-1}$ representing the star-forming objects while the other peak is found at $\mathrm{sSFR} \sim 10^{-12}\ \mathrm{yr}^{-1}$ representing the quenched population. Furthermore, we compare our observations with the predictions from the IllustrisTNG and Illustris simulations and affirm that the "TNG" model performs much better than its predecessor. However, we show that the simulated SFRF and CSFRD of TNG simulations are highly dependent on resolution, reflecting the limitations of the model and today's state-of-the-art simulations. We demonstrate that the bimodal, two peaked sSFRF implied by the SDSS observations does not appear in TNG regardless of the adopted box-size or resolution. This tension reflects the need for inclusion of an additional efficient quenching mechanism in the TNG model.

Key words: methods: statistical — galaxies: formation — galaxies: distances and redshifts — hydrodynamics

1 INTRODUCTION

The star formation rate (SFR) taking place in galaxies and across the Cosmos represents a fundamental constraint for galaxy formation physics and stellar evolution models. The number density of star-forming galaxies as a function of their SFR, i.e. the star formation rate function (SFRF), provides qualitative and quantitative information about star formation occurring in galaxies, while by definition its integration results in the cosmic star formation rate density (CSFRD).

To obtain the SFRs of galaxies, observational studies typically have to rely on models which provide correlations between SFR and the observed ultraviolet (UV) (Santini et al. 2017; Blanc et al. 2019), infrared (IR) (Whitaker et al. 2014; Guo et al. 2015), Hα (Cano-Díaz et al. 2019), O[II] emission (Lopez et al. 2020) and radio luminosities (Karim et al. 2011) or the spectral energy distribution (SED) fitting method (Duncan et al. 2014; Kurczynski et al. 2016; Trčka et al. 2020). Some studies in the literature rely on more than one indicator/methodology to provide a multi-wavelength analysis (Davies et al. 2019; Katsianis et al. 2019), with some finding discrepancies between the different techniques (Davies et al. 2016; Katsianis et al. 2017a) and others not (Madau & Dickinson 2014; Driver et al. 2016). Nevertheless, most of the studies in the literature acknowledge that every single methodology has advantages but at the same time shortcomings (Lee et al. 2009; Katsianis et al. 2020). For example, UV light is subject to dust attenuation effects (Dunlop et al. 2017; Baes et al. 2020) and is usually not complete for bright high star-forming galaxies. It provides information for intermediate and low star-forming galaxies at high redshifts ($z > 2$) but is not that successful at lower redshifts (Katsianis et al. 2017b). On the other hand, the IR luminosity originating

from dust continuum emission is a good tester of dust physics (Hirashita et al. 2003; Katsianis et al. 2016) with IR wavelengths (especially mid-IR and far-IR) being utilized to determine the total IR luminosity. Severe drawbacks of IR studies though are that (a) they usually do not have sufficient wavelength coverage (Lee et al. 2013; Pearson et al. 2018), (b) can be compromised by Active Galactic Nuclei (AGNs, Roebuck et al. 2016; Brown et al. 2019), (c) have to rely on SED libraries (Dale & Helou 2002; Wuyts et al. 2008), which have been constructed from galaxies at low redshifts and are not reliable at higher redshifts, and (d) other sources can contribute to the heating of dust in galaxies and this contribution can be falsely taken as star formation, for example, old stellar populations can significantly contribute to dust heating, complicating the relation between SFR and IR emission (Viaene et al. 2017; Nersesian et al. 2019). Besides UV and IR, Hα photons can also be applied to trace the intrinsic SFRs. However, Hα radiation is subject to severe dust attenuation effects, can usually probe intermediate star-forming objects (Katsianis et al. 2017a) and is usually incomplete for high star-forming systems. Due to the above limitations of SFRs derived from monochromatic luminosities, other studies employ the SED fitting techniques on numerous bands (Leja et al. 2019; Hunt et al. 2019). However, Katsianis et al. (2015) and Santini et al. (2017) suggested that this method suffers from parameter degenerations, which are serious for the SFR estimation. Besides the fact that SFR represents an excellent and direct instantaneous census of star formation, most articles, instead of focusing on the SFRF, usually examine the stellar mass function (SMF) which involves an integrated property with time.

Cosmological simulations are a valuable tool to investigate galaxy formation since the story of the Universe involves high complexity originating from different astrophysical processes, like the nonlinear evolution of dark matter halos, feedback, gas heating/cooling and chemical processes. Cosmological-scale simulations such as Illustris (Vogelsberger et al. 2014), Blue Tides (Feng et al. 2016), Horizon-AGN (Kaviraj et al. 2017), Mufasa (Davé et al. 2017), Romulus (Tremmel et al. 2017), IllustrisTNG (Springel et al. 2018; Pillepich et al. 2018b) and SIMBA (Davé et al. 2019) implement subgrid models to reproduce stellar, gaseous and black hole components that attempt to resemble those in observed galaxies. Moreover, semi-analytic models like the Durham model (Cole et al. 2000), L-GALAXIES (Guo et al. 2013), GALACTICUS (Benson 2014) and SHARK (Lagos et al. 2018) have enabled studying galaxy formation in larger volumes. More specifically, the evolution of the SFRF has been examined by some hydrodynamic simulations (Davé et al. 2011; Tescari et al. 2014; Katsianis et al. 2017a; Davé et al. 2017; Cañas et al. 2019) and semi-analytic models (Fontanot et al. 2012; Gruppioni et al. 2015) at different redshifts. Tescari et al. (2014) and Katsianis et al. (2017a) demonstrated the importance of feedback from supernovae (SNe) and AGNs in the evolution of the SFRF for $z \sim 1-7$ galaxies. Gruppioni et al. (2015) compared semi-analytic models (e.g. Monaco et al. 2007; Henriques et al. 2015) with IR observations. The comparison indicated that semi-analytic models underpredict the bright end of the SFRF at intermediate and high redshifts. Davé et al. (2017) compared Mufasa to observed galaxy SFRs and sSFRs. At $z = 0$, the simulated SFRF is in good agreement with Bothwell et al. (2011) but has higher normalization by up to $\sim \times 3$ in comparison with the Gunawardhana et al. (2013) data from the Galaxy And Mass Assembly (GAMA) survey. The authors also compared the simulated specific star formation rate functions (sSFRFs) with the observed sSFRF given by Ilbert et al. (2015) demonstrating a good agreement in most stellar mass bins. Last, Katsianis et al. (2017b) demonstrated that the SFRF of the EAGLE reference simulation is in good agreement with the UV and Hα observations at $z = 0$, while distributions that originate from IR and radio data suggest a higher number density of high star-forming systems. The authors demonstrated that the reason for this inconsistency is the presence of the AGN feedback in EAGLE, which is thought to be important in reproducing the UV and Hα data.

The Sloan Digital Sky Survey Data Release 7 (SDSS DR7; York et al. 2000; Strauss et al. 2002; Stoughton et al. 2002; Abazajian et al. 2009) is one of the most successful and well-studied galaxy redshift surveys for the local Universe. Its spectroscopic nature enables accurate redshift and infers stellar mass and SFR well for more than half of millions of galaxies. Therefore, SDSS DR7 provides a good opportunity to construct SFRFs, sSFRFs and cosmic SFR densities for the local Universe (Yang et al. 2013). The above can be compared with previous studies that employed different SFR indicators and techniques and provide further constraints on cosmological simulations and semi-analytic models. Besides, Illustris and its successor IllustrisTNG represent two state-of-the-art cosmological hydrodynamic models that have been successful at reproducing numerous observations. It would be interesting to perform a direct comparison with the observed SFRFs and sSFRFs from the observations, and point out any agreements or inconsistencies.

The observed SFRF, due to the uncertainties on SRF estimation, inevitably suffers from the so-called Eddington bias (Eddington 1913). The Eddington bias simply describes the fact that when counting the number

of galaxies in bins of galaxy properties (e.g., luminosity, stellar mass, SFR and host halo mass), errors in the estimation of the properties lead to potential biases in the histograms (e.g., luminosity function; SMF (Caputi et al. 2011; Ilbert et al. 2013) or halo mass function (Dong et al. 2019)). The extent of the Eddington bias depends on the size of errors and the shape of the histograms. For instance, at the exponential cutoff part, there will be significantly more galaxies scattering from lower bins to higher ones than the reverse, which severely biases the density of luminous/massive galaxies. In the context of SFRF, it would be expected that the density of high star-forming galaxies is overestimated. Therefore, applying the observed Eddington-biased SFRF directly computed from the observations would prevent us from a fair comparison with the predictions from cosmological simulations, especially at the high star-forming end.

The structure of the paper is as follows: In Section 2, we will present and test our methodology for correcting the Eddington bias on SFR function and infer the intrinsic SFRFs and sSFRFs for SDSS DR7. In Section 3, we introduce briefly the Illustris and IllustrisTNG suite of simulations and compare these with the SFRFs and sSFRFs from SDSS DR7. We summarize and discuss our conclusions in Section 4. Throughout the work, we adopt a spatially flat Λ cold dark matter cosmology with $\Omega_{\rm m} = 0.275$ (WMAP7; Komatsu et al. 2011) to convert the redshift to comoving distance. To facilitate fair comparisons on the SFRFs and sSFRFs, we convert using the corresponding Hubble constants adopted by the various simulations and observations employed in this work. We write $\log$ for base-10 logarithm.

2 A METHOD FOR CORRECTING THE EDDINGTON BIAS ON THE STAR FORMATION RATE FUNCTION AND SPECIFIC STAR FORMATION RATE FUNCTION

The galaxy properties (e.g., magnitude and redshift) considered in this work are obtained from the New York University Value-Added Galaxy Catalog (NYU-VAGC; Blanton et al. 2005). We adopt the SFRs, specific star formation rates and their uncertainties provided by the MPA-JHU group[1]. The SFRs are computed by fitting the emission lines (e.g., Hα, Hβ, [O III]5007, [N II]6584, [O II]3727 and [S II]6716) with Bayesian methodology and model grids (see details in Brinchmann et al. 2004). The stellar masses of galaxies are taken from Kauffmann et al. (2003), who estimated these by applying two stellar absorption-line indices, the 4000 Å break strength, and the Balmer absorption-line index Hδ_A. The specific star formation rates are simply calculated by combining the SFR and stellar mass likelihoods aforementioned. Throughout this work, we take the median values from the SFR/sSFR posterior probability distributions as our best values. When taking into account cases with asymmetric probability distributions, we estimate the uncertainties as the mean 34th percentiles from the median given 16th and 84th percentiles of probability distributions. In detail, these uncertainties are mostly from degenerations produced in the SED fitting and also include different sources of errors, such as the photometric errors, the wavelength coverage and the limited SED template grids. A Kroupa (2001) initial mass function is assumed in the derivation of the quantities. All the source data we used in this work are compiled here[2].

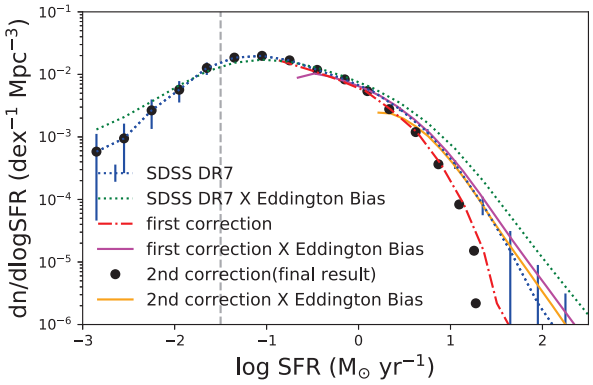

Fig. 1 The Eddington bias correction on the SFRF in SDSS DR7. The blue (*green*) dashed line represents observed SFRF computed from SDSS DR7 (observed SFRF convolving with SFR uncertainties). The red dash-dotted line (*black dots*) is/are the first (*second*) correction, and the magenta (*orange*) solid line is the first (*second*) correction plus Eddington bias. Based on the definition of Eddington bias, the second correction ought to be the intrinsic SFRF we are seeking. The flattening behavior on the left side of first/second correction plus Eddington bias line is totally artificial since when plotting, we only build the histogram with galaxies with updated SFRs. If taking all galaxies into account, both left sides will form a line on top of SDSS DR7 (see magenta and yellow solid lines in Fig. A.1). See details in Sect. 2.1. The error bars on the observed SFRF are computed from 150 jackknife samples (Xu et al. 2016, 2018). The grey vertical dashed line marks the complete boundary for the observations and simulations, and on its right forms the analysis of this work.

2.1 The Eddington Bias Correction on Star Formation Rate Function and Beyond

In this subsection, we present and test our method for correcting the Eddington bias in SFRF. We start with the

[1] https://wwwmpa.mpa-garching.mpg.de/SDSS/DR7/sfrs.html

[2] http://gax.sjtu.edu.cn/data/Group.html

observed SFRF computed following the so-called 1/Vmax weighting method (Felten 1976; Li & White 2009) to correct the Malmquist bias due to the flux-limited survey nature. We note that Vmax is calculated from r-band Petro magnitude (K+E corrected to z=0.1), with spectroscopy completeness also taken into account.

Since the observed SFRF is a result of convolution between the intrinsic SFRF and the uncertainties on SFRs, in principle, we can get rid of the Eddington bias by seeking a function such that, after convolving with the provided star formation rate uncertainties, the resultant function matches the observed SFRF. Motivated by this idea, we develop an empirical method to remove the Eddington bias by the following steps and each step is also illustrated in Figure 1.

(i) Step 1: We convolve the observed SFRF with the SFR uncertainties to obtain a function (dubbed "SDSS DR7 $\times$ Eddington bias" in Fig. 1). This new function can be understood as an SFRF observed in a world contaminated by the Eddington bias *twice*. Here and after, by convolving SFRF (or SMF in the later section) with SFR (stellar mass) uncertainties, in practice, we draw 1000 SFRs (stellar masses) for each galaxy with the assumption that each galaxy follows a Gaussian distribution around its median SFR (stellar mass) and its uncertainty is the standard deviation. We then build a histogram of 1000 mocks and take the median value in each bin as the bin value. By doing this, we effectively inject the Eddington bias effect.

(ii) Step 2: After recording the difference in the x-axis ($\log$ SFR) between the observed SFRF and "SDSS DR7 $\times$ Eddington bias" as a function of x-coordinates of observed SFRF, we interpolate and apply the "correction" to the individual galaxy SFRs to effectively remove the Eddington bias on the level of individual galaxies. With updated SFRs for all the galaxies, we are ready to build the histogram of a new SFRF labeled "first correction" SFRF. We note that the galaxies with SFR $\leq 10^{-0.2}$ $\mathrm{M_\odot\,yr^{-1}}$ by design do not need to be corrected for Eddington bias, while the starburst galaxies (SFR ≥ 10 $\mathrm{M_\odot\,yr^{-1}}$) require a considerable correction.

(iii) Step 3: We then convolve the "first correction" SFRF with the SFR uncertainties again to obtain the so-called "first correction $\times$ Eddington bias" SFRF function. For simplicity, we assume that the galaxy SFR uncertainties stay the same regardless of their change in SFRs.

(iv) Step 4: If the "first correction $\times$ Eddington bias" function matches the observed SFRF, it implies that the "first correction" should be the intrinsic Eddington-bias-free SFRF. If not, as our SFRF case shows in Fig. 1, we go back to Step 2 by recording the difference in the x-axis between the observed SFRF and "*first correction $\times$ Eddington bias" function* as a function of x-coordinates of observed SFRF. We interpolate and apply this additional "correction" to the already updated SFRs of all galaxies. We then plot the "2nd correction" SFRF with the twice updated SFRs. Note that the first (second, ..., Nth) corrections that were applied to the individual galaxy SFRs should always come from the difference in the x-axis between the observed SFRF and "*first (second, ... , Nth) correction $\times$ Eddington bias" function* as a function of x-coordinates of observed SFRF. These corrections should be asymptotic to 0, as the "first (second, ... , Nth) correction $\times$ Eddington bias function" converges to the observed SFRF.

(v) Step 5: We repeat step 3 but convolve the "2nd correction" SFRF with the SFR uncertainty. After that, repeat steps 4 and 5 until the "N-th correction $\times$ Eddington bias" function matches the observed SFRF.

The intrinsic SFRF can be found by iteratively applying these steps until the "N-th correction $\times$ Eddington bias" function matches the observed SFRF. For our SFRF case, it only takes us two iterations to arrive at the Eddington-bias-free SFRF, plotted in Fig. 1. We note that by no means do we declare our method as an exact method for recovering the intrinsic SFRF due to many approximations and simplifications used in the assumptions and detailed procedures. However, we believe that, to the zeroth-order correction, the function inferred from this method ought to be much closer to the intrinsic SFRF than the observed SFRF.

To ensure that our method recovers (or at least approaches as closely as possible) the intrinsic SFRF, we test our method in the TNG100–1 simulation in Appendix A. In short, our method for correcting the Eddington bias in SFRF is demonstrated to work as expected in the simulation, with the simplest configuration though. The test gives us strong confidence in our inference on the SDSS DR7 intrinsic SFRF. In principle, our method can be applied to any Schechter-like histogram, such as luminosity function and SMF. Compared to the previous work on correcting the Eddington bias on SMF (Caputi et al. 2011; Ilbert et al. 2013), our method has much more flexibility since we do not assume a functional form for the SMF (we also apply our method to the SMF in Appendix B). The intrinsic SFRF of the local Universe is listed in Table 1 and is also represented as black points in Figure 2.

2.2 The Intrinsic Star Formation Rate Function

In Figure 2, we present a comparison between our results from SDSS DR7 with the SFRFs given by Katsianis et al. (2017b). We demonstrate that the intrinsic

SFRF from our analysis is overall in good agreement with the SFRF derived from the UV luminosity function of Robotham et al. (2011), especially when the comparison is made below the SFR limit of $5\,\mathrm{M}_\odot\,\mathrm{yr}^{-1}$. However, at the high star-forming end ($\mathrm{SFR} > 10\,\mathrm{M}_\odot\,\mathrm{yr}^{-1}$), the intrinsic SFRF lies between the SFRFs obtained from the UV data and the IR data from Patel et al. (2013). As mentioned in the Introduction, UV light is subject to dust attenuation effects. This usually makes UV studies incomplete at the bright end since high star-forming objects with huge contents of dust will not be present in the survey. Besides, since dust attenuation effects become more severe for high star-forming objects, any applied dust corrections to infer the intrinsic SFRs can be underestimated (Meurer et al. 1999; Katsianis et al. 2020). Both effects can result in underestimated SFRFs at the high star-forming end from UV data. On the other hand, IR light can be enhanced by other sources (e.g. old stellar populations, AGNs) and this augmentation can be falsely taken as additional star formation, especially in massive/old galaxies. The above can result in overestimated IR SFRFs at the high star-forming end. The SED derived SFRF from SDSS DR7 lies between the distributions from UV and IR data, possibly demonstrating both that the UV SFRFs are (slightly) underestimated while IR SFRFs are overestimated. We perform the comparison of the SDSS DR7 SFRFs with the Illustris and IllustrisTNG simulations in Section 3.2.

The decline in the number density of galaxies below $\mathrm{SFR} = 10^{-1.5}\,\mathrm{M}_\odot\,\mathrm{yr}^{-1}$ displayed in Figure 2 is associated with the fact that the survey is incomplete and unable to detect numerous faint/low star-forming objects. The decline in the SDSS SFRF below this limit is not a behavior driven from physical reasons since the UV constraints given by Katsianis et al. (2017b) probe the SFRF to up to $10^{-2}\ \mathrm{M}_\odot\,\mathrm{yr}^{-1}$ and predictions from cosmological simulations like EAGLE do not manifest this behavior and demonstrate a Schechter form. Thus, we set our confidence limit in SDSS in terms of galaxy SFRs at $10^{-1.5}\,\mathrm{M}_\odot\,\mathrm{yr}^{-1}$. The limit of SDSS in terms of the stellar mass is set at 10^9 $\mathrm{M}_\odot$ (Weigel et al. 2016).

2.3 The Intrinsic Specific Star Formation Rate Function

A direct measurement of the connection between galaxy SFRs and stellar masses involves the specific star formation rate (Brinchmann & Ellis 2000), defined as the SFR per unit stellar mass M^*, i.e., $\mathrm{sSFR} = \mathrm{SFR}/\mathrm{M}^*$. The sSFR of a galaxy is a key property commonly implemented in the literature to distinguish if the galaxy is star-forming or quenched. It is a common practice to define the passive population as galaxies with sSFR lower than

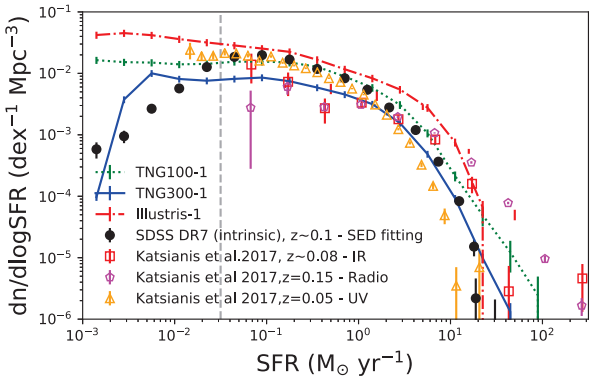

Fig. 2 The SFRFs of the local Universe: The green dotted line represents the SFRFs derived from TNG100, the blue solid line is from TNG300-1 and the red dash-dotted line is from Illustris-1. The black filled dots represent the intrinsic SFRFs inferred from SDSS DR7 (Eddington bias removed, see text for details), the empty red squares, magenta pentagons and orange triangles show observed SFRFs obtained via tracers as IR, radio and UV luminosity functions, respectively. The error bars on SDSS DR7 SFRF are obtained by the 150 jackknife subsamples.

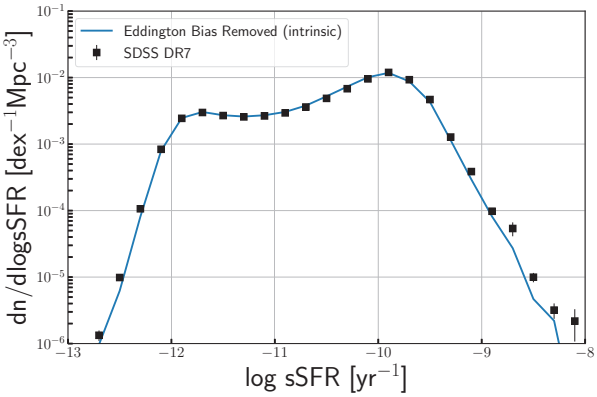

Fig. 3 The Eddington bias correction on specific star formation rate in SDSS DR7. The black dots represent the observed sSFRF while the blue line is the Eddington bias corrected sSFRF. The error bars on the observed sSFRF are computed from 150 jackknife samples.

$10^{-11}\,\mathrm{yr}^{-1}$ (Ilbert et al. 2015; Katsianis et al. 2020). Thus, constructing the sSFRF enables us to study quantitatively and qualitatively the distribution of the quenched and star-forming objects in SDSS DR7 and simulations.

Following the steps laid out in Section 2.1, one could have applied the methodology to the observed sSFRF. However, the shape of the sSFRF (bimodal form, depicted in Fig. 3) raises the difficulty of applying our method, which works only for a Schechter-like function.

Instead, by utilizing the by-products of SFRF Eddington bias correction procedures, i.e., the approximated Eddington bias corrected SFRs for the individual galaxy, one would immediately have the Eddington-bias-

Table 1 The Intrinsic SFRF of SDSS DR7

log SFR $[\mathrm{M_\odot\,yr^{-1}}]$	Comoving galaxy number density $[\mathrm{dex^{-1}\,Mpc^{-3}}]$	Error $[\mathrm{dex^{-1}\,Mpc^{-3}}]$
−2.85	5.82×10^{-4}	1.71×10^{-4}
−2.55	9.48×10^{-4}	2.16×10^{-4}
−2.25	2.66×10^{-3}	4.10×10^{-4}
−1.95	5.69×10^{-3}	6.70×10^{-4}
−1.65	1.27×10^{-2}	9.34×10^{-4}
−1.35	1.85×10^{-2}	9.02×10^{-4}
−1.05	1.98×10^{-2}	8.23×10^{-4}
−0.75	1.68×10^{-2}	5.20×10^{-4}
−0.45	1.18×10^{-2}	3.11×10^{-4}
−0.15	8.32×10^{-3}	2.07×10^{-4}
0.10	5.41×10^{-3}	1.21×10^{-4}
0.33	2.78×10^{-3}	6.34×10^{-5}
0.62	1.20×10^{-3}	4.40×10^{-5}
0.87	3.66×10^{-4}	1.81×10^{-5}
1.10	8.33×10^{-5}	7.82×10^{-6}
1.26	1.51×10^{-5}	4.60×10^{-6}
1.27	2.19×10^{-6}	2.41×10^{-6}
1.48	5.01×10^{-7}	1.59×10^{-6}
1.93	1.98×10^{-7}	3.45×10^{-7}
1.97	3.81×10^{-8}	1.96×10^{-7}

The first column is the SFRs, and the second (third) column represents the corresponding comoving galaxy number densities (errors). The error bars are obtained by 150 jackknife samples.

free sSFRs for each galaxy once the stellar mass is corrected for the Eddington bias as well. Luckily, the SMF also follows a Schechter function shape and it allows us to apply our method to the SMF so that we could obtain approximated Eddington-bias-corrected stellar masses for each galaxy

We correct the Eddington bias in the SMF in Appendix B (see Fig. B.1). Note that our method is robust in terms of recovering the intrinsic SFRF/SMF, as demonstrated in Section 2.1. However, it is not necessarily exact in extracting the correction down to the level of individual galaxies. As an approximation, we support that it is a valid approach to do Eddington bias corrections for the case of sSFRF.

The inferred Eddington-bias free sSFRF is shown in Figure 3, which is almost identical to that without Eddington bias correction, except at the very active star-forming regime ($\mathrm{sSFR} \sim 10^{-8}\,\mathrm{yr^{-1}}$). The similarity between the two sSFRs is probably due to the cancelation of the Eddington bias in both SFRF and SMF. We limit our analysis to galaxies with $\mathrm{SFR} > 10^{-1.5}\,\mathrm{M_\odot\,yr^{-1}}$ and stellar mass $\mathrm{M_\star} > 10^9\,\mathrm{M_\odot}$ for completeness.

3 COMPARISON WITH COSMOLOGICAL SIMULATIONS

3.1 The IllustrisTNG Simulations

Illustris-1 (Vogelsberger et al. 2014) consists of a cosmological simulation run with the moving-mesh code AREPO (Springel 2010). It includes sophisticated sub-grid physics that involve gas cooling, sub-resolution interstellar medium modeling, stochastic star formation, stellar evolution, gas recycling, chemical enrichment, kinetic stellar feedback driven by SNe explosions, supermassive black hole (SMBH) growth and related AGN feedback. The IllustrisTNG (Weinberger et al. 2017; Pillepich et al. 2018b) project is the successor of the Illustris simulations and includes an updated galaxy formation model that employs new physics and numerical improvements to address some shortcomings of the original Illustris-1 model (Pillepich et al. 2018b). Some key and notable improvements relevant to our work are:

- An updated kinetic AGN feedback model for objects with low accretion rates in the form of a kinetic, supermassive driven wind (Weinberger et al. 2017). The above implementation enhances feedback, especially for objects with $10^{12} - 10^{14}\,M_\odot$ halo masses, and decreases the simulated stellar masses for the TNG100 model bringing observed and simulated SMFs into better agreement (Pillepich et al. 2018b). In contrast, Illustris reproduced an SMF with higher values at $z < 1$.
- An improved parameterization of galactic winds (Pillepich et al. 2018b). Differently from Illustris, winds are injected isotropically, with larger wind Velocity and Energy Factors. The new feedback implementation solved the mild decline in the CSFRD of the original Illustris model at $z < 1$ and played a major role in shaping the SMF of low mass objects with $\mathrm{M_\star} < 10^{10}\,\mathrm{M_\odot}$.
- The updated TNG model produces the observed color bimodality. Nelson et al. (2018) demonstrated that the

simulated $(g-r)$ colors of TNG galaxies at low redshift are in good agreement with a quantitative comparison to observational data from SDSS at $z < 0.1$. The authors obtained the locations in the color of both the red and blue populations at the color $-$ $M_\star$ plane, the relative strength between the red and blue distributions considering histograms of $(g-r)$ colors, the location of the color minimum between the two populations, and the location of the maximal point of the bimodality. The authors suggested that this is the result of the updated feedback prescriptions in the improved next-generation model.

The TNG300–1 and TNG100–2 simulations are performed at a factor of 8 lower in mass and 2 at spatial resolution when compared to the TNG100 run. Otherwise all three configurations adopt an identical model with the same parameters for their sub-grid models regardless of box-size and resolution. TNG100 has a similar resolution as the original Illustris simulation so we can perform a direct comparison between them. More details on the simulations are summarized in Table 2.

3.2 IllustrisTNG Star Formation Rate Function and Cosmic Star Formation Rate Density

In Figure 2 we demonstrate that the Illustris SFRF has a higher normalization with respect to our SDSS observations at all SFR regimes, while the TNG100–1 simulation performs much better, especially for objects with low SFRs. The reason for this is that the updated TNG model includes a range of improvements (e.g. on the AGN feedback and galactic winds schemes) to decrease the simulated stellar masses and CSFRD at $z < 1$. We demonstrate that the TNG100–1 SFRF has good agreement with the SDSS observations for objects with $\mathrm{SFR} = 0.01 - 5\,\mathrm{M}_\odot\,\mathrm{yr}^{-1}$. However, the TNG model does not reproduce our SDSS observations at the high star-forming end and typically lies between the UV and IR constraints given in Katsianis et al. (2017b). In other words, TNG300–1 reproduces the observed SDSS SFRF at the $\mathrm{SFR} > 5\,\mathrm{M}_\odot\,\mathrm{yr}^{-1}$ regime. It would be intriguing to suggest that this agreement happens since the TNG300-1 simulation has a larger box-size and thus can sample a larger number of objects, employ better statistics and is more trustworthy at the high star-forming end, making the effects of finite box-size less severe. However, this good agreement between TNG300–1 and SDSS at the high star-forming end is a matter of coincidence and an effect of low resolution (more details can be found in Appendix C). In Appendix D, we also calculate the CSFRD in the local Universe, since it is a cosmic metric for star formation usually employed in the literature, and perform further resolution and box-size tests.

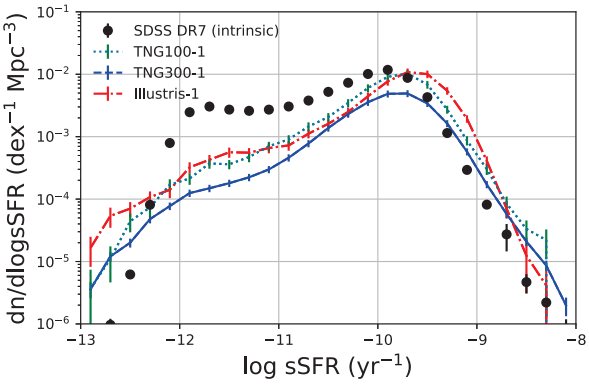

Fig. 4 The specific star formation rate of simulations and observation: the green dashed line represents the sSFRF derived from TNG100–1, the blue solid line from TNG300–1 and the red dash-dotted line from Illustris-1. The black filled dots are intrinsic sSFRF inferred from SDSS DR7, with correction for the Eddington bias (see subsection 2.3 for details), and the error bars are obtained by the jackknife method.

3.3 The IllustrisTNG Specific Star Formation Rate Function

The fact that TNG-100 can reproduce consistent SFRFs and SMFs with SDSS does not necessarily mean that this is achieved with simulated galaxies that each uniquely fulfills the observed relation between SFR and stellar mass. We investigate how the simulated sSFRF from the Illustris and IllustrisTNG simulations compares with SDSS in Figure 4. We impose the same limits on the simulations ($\mathrm{SFR} > 10^{-1.5}\,\mathrm{M}_\odot\,\mathrm{yr}^{-1}$ and stellar mass $\mathrm{M}_\star > 10^9\,\mathrm{M}_\odot$). We see that both the observed and simulated distributions have a peak at $\mathrm{sSFR} \sim 10^{-9.7}\,\mathrm{yr}^{-1}$. These galaxies would be classified as star-forming objects and it is encouraging that TNG can qualitatively reproduce this behavior. We note that this is found by the model regardless of resolution (more details can be found in the Appendix C)

The intrinsic sSFRF of SDSS DR7 displayed in Figure 4 demonstrates a clear bimodality. To be more specific, a second peak is detected at $\mathrm{sSFR} \sim 10^{-12}\,\mathrm{yr}^{-1}$ reflecting the presence of the quenched population of galaxies, which at redshift $z \sim 0$ is expected to be abundant. We note that this population does not appear in IllustrisTNG which does not exhibit the same qualitative behavior as a double peak. Quantitatively, the TNG run has almost an order of magnitude lower number density of objects with $\mathrm{sSFR} \sim 10^{-12}\,\mathrm{yr}^{-1}$ compared with the SDSS constraints. The reason for this tension possibly

Table 2 Primary Parameters of the Simulations Analyzed in This Study

Simulation Name (1)	Volume (Mpc^3) (2)	$\mathrm{N_{DM}}$ (3)	$\mathrm{m_{DM}}(10^6\,\mathrm{M_\odot})$ (4)	$\mathrm{m_{gas}}(10^6\,\mathrm{M_\odot})$ (5)	$\mathrm{N_{galaxy}}(z=0)$ (6)
Illustris-1	106.5^3	1820^3	6.3	1.3	4 366 546
TNG100–1	110.7^3	1820^3	7.5	1.4	4 371 211
TNG100–2	110.7^3	910^3	60	11	698 336
TNG100–3	110.7^3	455^3	480	89	118 820
TNG300–1	302.6^3	2500^3	59	11	14 485 709

Column (1): run name; Col. (2): box volume of the simulation; Col. (3): number of dark matter particles; Col. (4): mass of the dark matter particles; Col. (5): initial mass of the gas particles; Col. (6): number of galaxies at $z = 0$.

Table 3 Specific Star Formation Rate of SDSS

log sSFR $[\mathrm{yr}^{-1}]$	Comoving galaxy number density $[\mathrm{dex}^{-1}\,\mathrm{Mpc}^{-3}]$	Jackknife error $[\mathrm{dex}^{-1}\,\mathrm{Mpc}^{-3}]$
−12.9	4.32×10^{-7}	1.90×10^{-7}
−12.7	9.68×10^{-7}	2.42×10^{-7}
−12.5	6.20×10^{-6}	6.41×10^{-7}
−12.3	8.11×10^{-5}	4.99×10^{-6}
−12.1	7.92×10^{-4}	2.24×10^{-5}
−11.9	2.47×10^{-3}	6.50×10^{-5}
−11.7	3.04×10^{-3}	8.00×10^{-5}
−11.5	2.71×10^{-3}	7.17×10^{-5}
−11.3	2.59×10^{-3}	8.02×10^{-5}
−11.1	2.71×10^{-3}	9.58×10^{-5}
−10.9	3.04×10^{-3}	1.22×10^{-4}
−10.7	3.79×10^{-3}	1.55×10^{-4}
−10.5	5.23×10^{-3}	1.72×10^{-4}
−10.3	7.31×10^{-2}	1.97×10^{-4}
−10.1	1.01×10^{-2}	2.58×10^{-4}
−9.9	1.18×10^{-2}	3.09×10^{-4}
−9.7	8.76×10^{-3}	2.58×10^{-4}
−9.5	4.30×10^{-3}	1.32×10^{-4}
−9.3	1.14×10^{-3}	4.34×10^{-5}
−9.1	2.94×10^{-4}	3.60×10^{-5}
−8.9	8.15×10^{-5}	8.58×10^{-6}
−8.7	2.72×10^{-5}	1.27×10^{-5}
−8.5	4.68×10^{-6}	1.60×10^{-6}
−8.3	2.20×10^{-6}	8.32×10^{-7}
−8.1	8.01×10^{-8}	1.11×10^{-6}

The first column is the median value of the interval, the second column is corresponding number of galaxies and the last column is the error calculated by jackknife method.

reflects the need for inclusion of a different or more effective quenching mechanism. We note that there are no significant deviations in the sSFRFs of the TNG model from the original Illustris simulation.

4 CONCLUSIONS

In this work, we present the first Eddington-bias-free SFRF, CSFRD and sSFRF in the SDSS DR7. We compare the above observational constraints with the reference simulations of Illustris and IllustrisTNG. We include resolution tests and discuss the accomplishments and shortcomings of the models. In the following, we summarize the main results and conclusions of our analysis:

– Without resorting to assuming a functional form for the intrinsic (Eddington bias corrected) SFRF, we correct the Eddington bias on the SFRF and sSFRF by subtracting the SFR of each galaxy utilizing the average shift in the SFRF induced by the Eddington bias iteratively (Fig. 1). We test our method on a simulated Eddington biased SFRF from TNG100–1 and the inferred "intrinsic" SFRF matches well with the true SFRF (Fig. A.1). The test reflects the robustness of our method and, in principle, it could be generalized to any Schechter-like function. We apply the above method to the SDSS SFRF and compare our results with predictions from cosmological simulations and other SFR indicators.

– The SFRF constructed from the SED derived SFRs of the SDSS survey is in excellent agreement with the SFRFs obtained from UV luminosities for objects at the $\mathrm{SFR} \sim 0.01 - 5\,\mathrm{M_\odot\,yr^{-1}}$ regime presented

in Katsianis et al. (2017b). However, the high star-forming end ($\mathrm{SFR} > 10\,\mathrm{M}_\odot\,\mathrm{yr}^{-1}$) lies between the determinations of the UV and IR/radio tracers. For high SFRs, a tension between UV and IR indicators is established in the literature owning to either underestimations of UV SFRs or overestimations of the IR SFRs. The SDSS SED SFRF of this work is in good agreement with other SFR indicators, especially UV which is able to probe low star forming objects, up to $\mathrm{SFR} = 10^{-1.5}\,\mathrm{M}_\odot\,\mathrm{yr}^{-1}$. Thus we set our confidence limit for SFRs to this value.

– The simulated reference model of the IllustrisTNG labeled as TNG100-1 produces an SFRF that is consistent with the constraints of the SDSS data for objects in the $\mathrm{SFR} \sim 0.01 - 5\,\mathrm{M}_\odot\,\mathrm{yr}^{-1}$ regime, while it performs much better than the original Illustris model. This reflects the improvements taken into account in the updated TNG model, including the feedback prescriptions. However, the simulation does not perform equally well for higher star-forming objects ($\mathrm{SFR} > 10\,\mathrm{M}_\odot\,\mathrm{yr}^{-1}$) with observations having lower number densities. The configuration with 8 times lower resolution and ∼20 times larger volume (labeled as TNG300–1) demonstrates a better agreement at the high star-forming end, despite the fact that it is not as successful for low star-forming objects. However, the reason for this agreement is coincidental and has its roots in resolution effects, rather than the better statistics produced in the larger box-size (Appendix C). This resolution driven effect brings observed and simulated high star-forming ends in agreement for non-physically motivated reasons.

– We demonstrate that the intrinsic sSFRF from SDSS has two peaks and demonstrates a clear bimodality for objects with $\mathrm{SFR} > 10^{-1.5}\,\mathrm{M}_\odot\,\mathrm{yr}^{-1}$ and stellar mass $\mathrm{M}_\star > 10^9\,\mathrm{M}_\odot$. The one peak appears at $\mathrm{sSFR} \sim 10^{-9.7}\,\mathrm{yr}^{-1}$. These galaxies would be classified as star-forming objects. A second peak is detected at $\mathrm{sSFR} \sim 10^{-12}\,\mathrm{yr}^{-1}$ reflecting the presence of the quenched population of galaxies, which at redshift $z \sim 0$ is expected to be abundant (subsection 3.3).

– We note that the bimodal sSFRF implied by SDSS observations does not appear in TNG100–1 or TNG300–1. The simulations do not exhibit the same qualitative behavior and demonstrate only one peak for high star-forming objects at $\mathrm{sSFR} \sim 10^{-9.6}\,\mathrm{yr}^{-1}$. The TNG run has almost 1 order of magnitude lower number density of passive objects with $\mathrm{sSFR} \sim 10^{-12}\,\mathrm{yr}^{-1}$ with respect to observations. This tension may reflect the need for inclusion of an additional or more efficient quenching mechanism (subsection 3.3). We note that the normalization of the simulated sSFRF increases with resolution but its shape remains the same.

Acknowledgements The authors thank the anonymous referee for helpful comments that significantly improved the presentation of this paper. HX thanks the useful discussion with Jiajun Zhang and Zhaozhou Li. This work is supported by the National Natural Science Foundation of China (Nos. 11833005, 11890692 and 11621303), 111 project (No. B20019) and Shanghai Natural Science Foundation (No. 15ZR1446700). We gratefully acknowledge the support of the Key Laboratory for Particle Physics, Astrophysics and Cosmology, Ministry of Education and the Tsung-Dao Lee Institute.

Appendix A: A TEST OF THE EDDINGTON BIAS CORRECTION METHOD USING TNG100

To ensure that our method recovers (or at least approaches as closely as possible) the intrinsic SFRF, we test our method in the TNG100–1 simulation in Appendix A. The first step is to start with an Eddington-biased SFRF, which is the counterpart to the observed SFRF in the simulation. However, due to the lack of Eddington bias in simulation, we have to manually assign some uncertainties in SFR for all the simulated galaxies to mimic the observed SFRF. The observation suggests that the error in SFR should be dependent on SFR, but for simplicity, we assume a universal 0.4 dex uncertainty in their SFRs (the arithmetic mean of error for all the SDSS DR7 galaxies provided in the MPA-JHU catalog) for all galaxies. We note that assigning an SFR-dependent error in SFR would not change the main conclusion in this test. Given the simulated Eddington-biased SFRF and the assumed universal SFR uncertainties, we obtain the "intrinsic SFRF" by following the steps outlined in Section 2.1, which turns out to be an excellent match with the true SFRF directly from the simulation, as shown in Figure A.1.

Appendix B: THE EDDINGTON BIAS CORRECTED STELLAR MASS FUNCTION

Following the steps laid out in Section 2.1, we start with the stellar mass provided by the JHU-MPA group. It only takes one iteration to obtain the intrinsic SMF (see Fig. B.1).

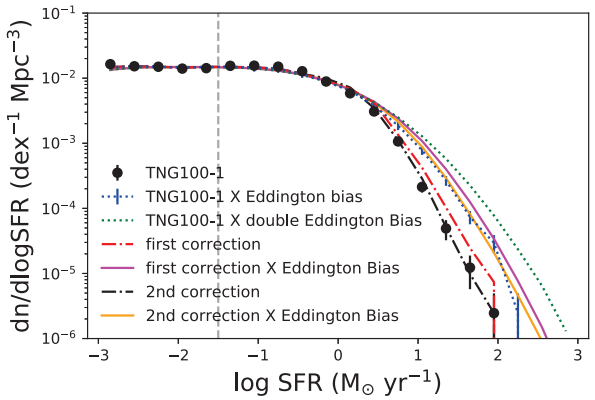

Fig. A.1 A test of our Eddington bias correction method on the SFRF using TNG100-1. The black dots represent intrinsic values from TNG100-1. The blue (green) dashed line signifies intrinsic values plus (twice) Eddington bias while the red (blue) dash-dotted line is the first (second) correction. Also, the magenta (orange) solid line is the first (second) correction plus Eddington bias. Based on our criteria in Step 5 of Section 2.1, the second correction should be the "intrinsic SFRF" and it matches that from the simulation well. The error bars displayed on the SFRFs are computed from 64 jackknife samples. To mimic the observation, the Eddington biased SFRF is computed from *only one* mock, which induces some wiggles in the curves. The twice Eddington biased and corrections convolved with Eddington bias SFRF is estimated from 1000 mocks. See details in Sect. 2.1.

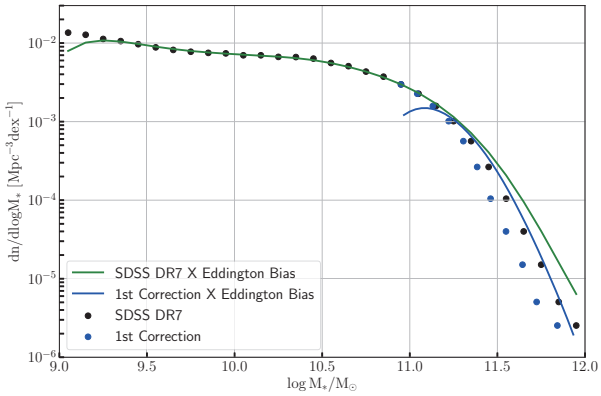

Fig. B.1 The Eddington bias correction on the SMF for SDSS DR7. The black dots represent the observed SFRF directly from SDSS DR7. The green (blue) solid line signifies the SDSS DR7 (first correction) plus Eddington bias. The blue dots correspond to the first correction and the intrinsic SMF we are seeking. The flattening behavior on the left side of blue solid line is totally artificial because we only build histograms with updated galaxy SFRs, the same as in Figure 1. See more details in Section 2.1 and Appendix B.

We note that a universal stellar mass error, ~ 0.15 dex (Li & White 2009; Yang et al. 2012), is assumed during the procedures.

Appendix C: RESOLUTION TEST AND BOX-SIZE TEST

In the left panel of Figure C.1, the comparison between TNG100–1 and TNG100–2 demonstrates that the simulated SFRF is highly dependent on resolution, even at the high star-forming end, and the TNG100–2 run has better agreement with the SDSS observations for objects with $\mathrm{SFR} > 5\,\mathrm{M}_\odot\,\mathrm{yr}^{-1}$. In the right panel of Figure C.1 we demonstrate that the TNG300–1 and TNG100–2 simulations reproduce identical results (both have the same resolution which is 8 times lower in mass than TNG100–1). The perfect agreement between TNG300–1 and TNG100–2 possibly reflects that the box-size of 100 Mpc is enough for studies of the CSFRD and SFRF in the TNG model. The complement of TNG100–1 simulation seems not affected significantly in terms of galaxy SFRs or low numbers of galaxies at the high star-forming end by the smaller box-size. However, the TNG100–1 and TNG100–2 simulations do not converge at any SFR regime, pointing to limitations in the model related to resolution.

We note that all TNG runs, regardless of resolution or box-size, utilize the default model parameter values given in Pillepich et al. (2018b) and no adjustments to resolution were done. Schaye et al. (2015) discussed the importance of re-scaling the parameters (especially feedback) of higher resolution simulations to produce properties and statistics of galaxies that converge with the lower resolution runs. The above convergence test (the agreement between the high resolution simulation with the one that adopts lower resolution and re-scaled parameters for sub-grid physics) was labeled by the authors as the "weak convergence" test, which EAGLE SFRFs satisfy (Katsianis et al. 2017b). The "strong convergence" test is only fulfilled when convergence between low and high resolution simulations is satisfied without any re-scaling of the parameters and consists of the ultimate test for the independence of the adopted cosmological model on the resolution. We demonstrate that the "strong resolution convergence" is not satisfied for the Illustris TNG SFRFs and the higher resolution TNG100-1 run does not converge with the TNG100–2 and TNG300-1 runs, having a larger normalization by 2 times at all SFRs regimes. Pillepich et al. (2018a) demonstrated that TNG100-1 and TNG300–1 SMFs would come into agreement by re-scaling the lower resolution simulation by a factor of 1.4. The authors emphasized that, while the incomplete resolution convergence of the SMFs of TNG300–1 with the TNG100–1 is without a doubt a limitation of the model, the needed re-scaling factor of 1.4 is relatively small and comparable with the current discrepancies across

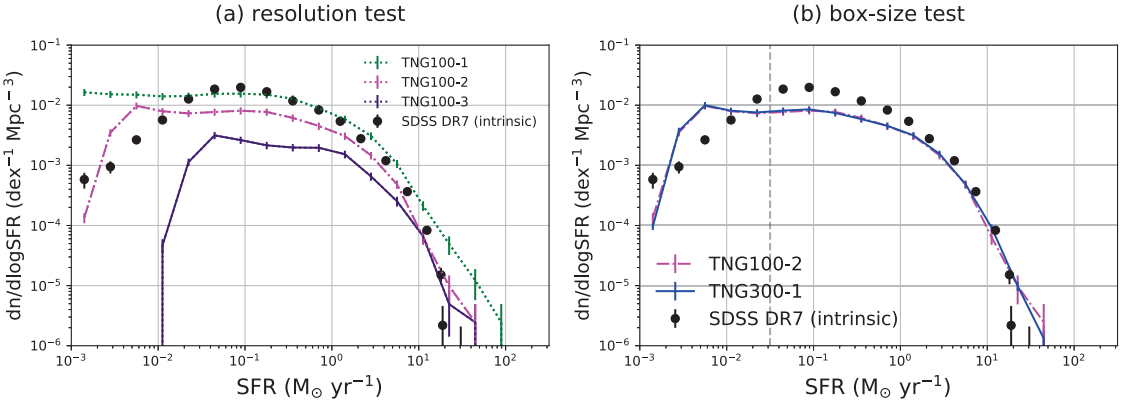

Fig. C.1 The SFRF between TNG simulations with different resolutions and box-sizes. (a) *Left panel*: This is a test that shows how the model varies with resolution as these three simulations have the same box-size but different particle masses. The green dotted line represents TNG100–1, the magenta dash-dotted line signifies TNG100–2, the indigo solid line corresponds to TNG100–3 and the black dots mark SDSS DR7. (b) *Right panel*: This is a test which demonstrates how the model varies with box-size as these two simulations have the same resolution but different volumes. The blue solid line represents TNG300-1, and the error bars in plots are obtained by the jackknife method.

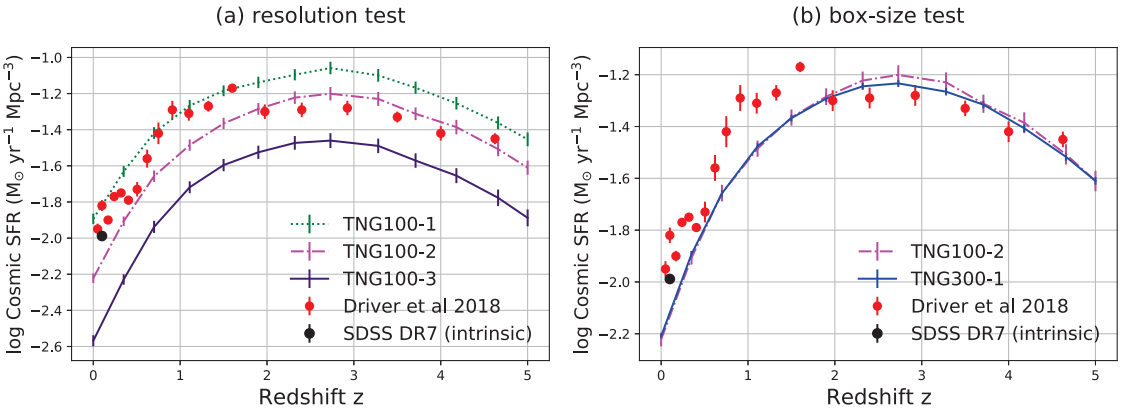

Fig. C.2 Comparison of the CSFRDs from different simulations. Similar to Fig. C.1, the *left panel* and *right panel* represent the resolution test and box-size test, respectively. The green dotted line signifies TNG100–1, the magenta dash-dotted line corresponds to TNG100–2, the indigo solid line means TNG100–3, the blue solid line represents TNG300–1, the black dot signifies the intrinsic value of SDSS DR7 and magenta dots mark observation data from Driver et al. (2018). The error bars in the plots are obtained by the jackknife method.

different observational measurements. In Figure C.1(a) we present the evolution of the TNG100–1 cosmic SFR density alongside the observations of Driver et al. (2018) and SDSS DR7 discussed in Section 2. We show that TNG100–1 is doing well against observations at $z < 1.4$. We note that the TNG model was tuned to do so, to surpass its successor, the original Illustris model that failed to reproduce the CSFRD at low redshifts. Besides the severe improvements, TNG100–1 implies higher values than observations at $z > 1.4$ and the TNG300–1 run performs better at earlier epochs with respect to the observations of Driver et al. (2018). We demonstrate that the agreement of TNG300–1 with high redshift observations is driven by resolution effects (Fig. C.1(b)) and that the strong convergence test is not fulfilled for the TNG100–1 and TNG300–1 CSFRDs, confirming that the problem of resolution effects goes beyond the $z \sim 0$ SFRF. We note that Pillepich et al. (2018b) performed resolution tests between simulations that adopted a 25 Mpc box and affirmed as well that higher resolutions resulted in higher CSFRDs in the TNG model. We also note that similar problems would be found in most cosmological simulations including EAGLE and are not only specific for TNG. Three serious concerns arise for cosmological simulations besides their great improvements in the last 10 yr from our analysis:

– 1) Current state-of-the-art cosmological simulations can reproduce a range of observations (e.g. SFRF) mostly because there is a proper tuning of the parameters of their model at the *adopted resolution*. If

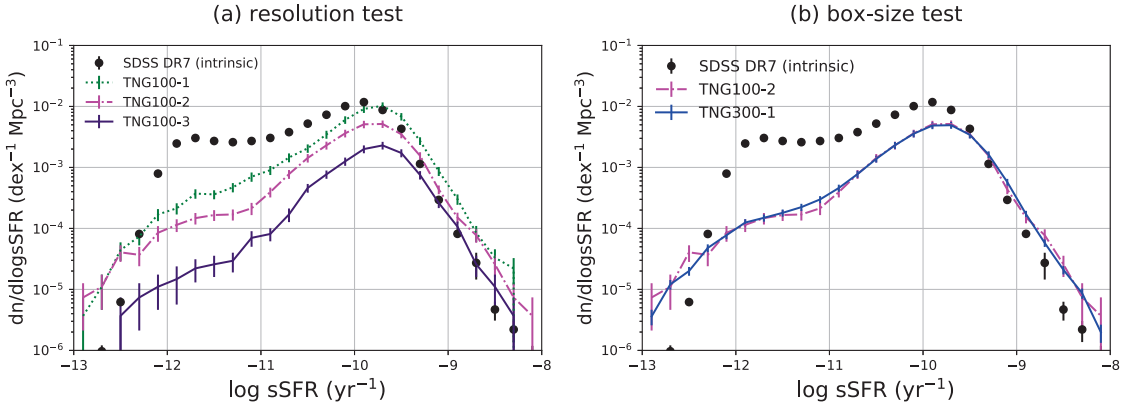

Fig. C.3 (a) This is a resolution test: The green dotted line represents TNG100–1, the magenta dash-dotted line signifies TNG100–2, the indigo solid line corresponds to TNG100–3 and the black dots from SDSS DR7 are attached for reference. (b) This is a box-size test. The blue solid line represents TNG300–1. The error bars in plots are obtained by the jackknife method.

the same model is run in lower resolution (regardless if it offers better statistics due to a larger box-size) it produces galaxies with different properties (e.g. lower SFRs). This brings the question: Is the model successful at the reference simulation (e.g. TNG100–1) for physical reasons? Or is it successful only for the adopted resolution and due to the tuning of parameters?

– 2) Good statistics of rare high star-forming galaxies are possible to be achieved in large box simulations (e.g. 205 Mpc). However, the large volume cannot alone validate a simulation to be applied as a predictive tool if we need to re-scale the properties and statistics of its galaxies due to limited resolution by the same level as the tension between observational studies. For example, the re-scaling needed between TNG300–1 and TNG100–1 SFRFs to bring them into an agreement at the high star-forming end is almost equal to the discrepancy between different SFR indicators (Katsianis et al. 2017b), so TNG300–1 cannot be relied on as a predictive simulation at the high star-forming end to distinguish between different observational studies and be a guide for future surveys.

– 3) Future simulations that will achieve higher resolutions and adopt current state-of-the-art models (e.g. TNG or EAGLE) will without doubt need to re-scale their current parameters for sub-grid physics and feedback to reproduce some observables. However, with proper re-scaling any of the above models at the adopted reference resolution will be able to reproduce critical constraints like the SMF and the evolution of the CSFRD. Which are the observables that can determine the success of a model? Should any comparisons be mostly qualitative instead of quantitative?

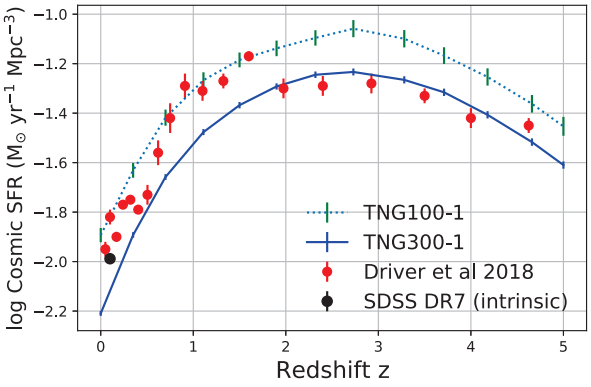

Fig. D.1 CSFRD: the green dotted line represents TNG100–1, blue solid line TNG300-1, magenta dots are the observations of Driver et al. (2018) and the black dot is the intrinsic CSFRD of SDSS DR7. The error bars are obtained by the jackknife method.

In Figure C.3, we demonstrate that the peak of sSFRF changes among different resolutions, since the TNG100–1 run has higher normalization by 2 times with respect the TNG100–2 configuration (left panel of Fig. C.3).

Appendix D: THE INTRINSIC LOCAL CSFRD

To obtain the CSFRD of the local Universe, a Schechter (1976) function is adopted to fit the inferred intrinsic SFRF displayed in Fig. 2

$$\frac{\mathrm{d}\phi}{\mathrm{dSFR}} = \phi_\star \left(\frac{\mathrm{SFR}}{\mathrm{SFR}^\star}\right)^\alpha \mathrm{e}^{-\mathrm{SFR}/\mathrm{SFR}^\star} \frac{1}{\mathrm{SFR}^\star} \qquad \text{(D.1)}$$

where α is the power-law slope of the low star-forming end and $\mathrm{SFR}^\star$ marks the characteristic SFR when the

function shape transits from power-law to exponential cutoff. The $\phi_\star$ is the function amplitude at $\mathrm{SFR}^\star$. We only fit the inferred intrinsic SFRF where we consider it to be complete, i.e., SFRs $\geq 10^{-1.5}\,\mathrm{M}_\odot\,\mathrm{yr}^{-1}$. The best-fit parameters we obtained are $\phi_\star = 2.61 \times 10^{-3} \pm 9.49 \times 10^{-5}\ \mathrm{Mpc}^{-3}$, $\mathrm{SFR}^\star = 2.89 \pm 0.07\ \mathrm{M}_\odot\,\mathrm{yr}^{-1}$ and $\alpha = -1.34 \pm 0.0115$. The intrinsic local CSFRD is therefore $9.74 \times 10^{-3} \pm 4.51 \times 10^{-4}\ \mathrm{M}_\odot\,\mathrm{yr}^{-1}\,\mathrm{Mpc}^{-3}$, as plotted in Fig. D.1 and Fig. C.2. We report the above in order to facilitate parameter studies of the SFRF (Smit et al. 2012; Tacchella et al. 2013) and CSFRD (Madau & Dickinson 2014; Davies et al. 2016).

References

Abazajian, K. N., Adelman-McCarthy, J. K., Agüeros, M. A., et al. 2009, ApJS, 182, 543
Baes, M., Trčka, A., Camps, P., et al. 2020, MNRAS, 494, 2912
Benson, A. J. 2014, MNRAS, 444, 2599
Blanc, G. A., Lu, Y., Benson, A., et al. 2019, ApJ, 877, 6
Blanton, M. R., Schlegel, D. J., Strauss, M. A., et al. 2005, AJ, 129, 2562
Bothwell, M. S., Kennicutt, R. C., Johnson, B. D., et al. 2011, MNRAS, 415, 1815
Brinchmann, J., Charlot, S., White, S. D. M., et al. 2004, MNRAS, 351, 1151
Brinchmann, J., & Ellis, R. S. 2000, ApJL, 536, L77
Brown, A., Nayyeri, H., Cooray, A., et al. 2019, ApJ, 871, 87
Cañas, R., Elahi, P. J., Welker, C., et al. 2019, MNRAS, 482, 2039
Cano-Díaz, M., Ávila-Reese, V., Sánchez, S. F., et al. 2019, MNRAS, 1830
Caputi, K. I., Cirasuolo, M., Dunlop, J. S., et al. 2011, MNRAS, 413, 162
Cole, S., Lacey, C. G., Baugh, C. M., & Frenk, C. S. 2000, MNRAS, 319, 168
Dale, D. A., & Helou, G. 2002, ApJ, 576, 159
Davé, R., Anglés-Alcázar, D., Narayanan, D., et al. 2019, MNRAS, 486, 2827
Davé, R., Oppenheimer, B. D., & Finlator, K. 2011, MNRAS, 415, 11
Davé, R., Rafieferantsoa, M. H., Thompson, R. J., et al. 2017, MNRAS, 467, 115
Davies, L. J. M., Driver, S. P., Robotham, A. S. G., et al. 2016, MNRAS, 461, 458
Davies, L. J. M., Lagos, C. d. P., Katsianis, A., et al. 2019, MNRAS, 483, 1881
Dong, F., Zhang, J., Yang, X., et al. 2019, ApJ, 883, 155
Driver, S. P., Wright, A. H., Andrews, S. K., et al. 2016, MNRAS, 455, 3911
Driver, S. P., Andrews, S. K., da Cunha, E., et al. 2018, MNRAS, 475, 2891
Duncan, K., Conselice, C. J., Mortlock, A., et al. 2014, MNRAS, 444, 2960
Dunlop, J. S., McLure, R. J., Biggs, A. D., et al. 2017, MNRAS, 466, 861
Eddington, A. S. 1913, MNRAS, 73, 359
Felten, J. E. 1976, ApJ, 207, 700
Feng, Y., Di-Matteo, T., Croft, R. A., et al. 2016, MNRAS, 455, 2778
Fontanot, F., Cristiani, S., Santini, P., et al. 2012, MNRAS, 421, 241
Gruppioni, C., Calura, F., Pozzi, F., et al. 2015, MNRAS, 451, 3419
Gunawardhana, M. L. P., Hopkins, A. M., Bland-Hawthorn, J., et al. 2013, MNRAS, 433, 2764
Guo, K., Zheng, X. Z., Wang, T., & Fu, H. 2015, ApJL, 808, L49
Guo, Q., White, S., Angulo, R. E., et al. 2013, MNRAS, 428, 1351
Henriques, B. M. B., White, S. D. M., Thomas, P. A., et al. 2015, MNRAS, 451, 2663
Hirashita, H., Buat, V., & Inoue, A. K. 2003, A&A, 410, 83
Hunt, L. K., De Looze, I., Boquien, M., et al. 2019, A&A, 621, A51
Ilbert, O., McCracken, H. J., Le Fèvre, O., et al. 2013, A&A, 556, A55
Ilbert, O., Arnouts, S., Le Floc'h, E., et al. 2015, A&A, 579, A2
Karim, A., Schinnerer, E., Martínez-Sansigre, A., et al. 2011, ApJ, 730, 61
Katsianis, A., Tescari, E., Blanc, G., et al. 2017a, MNRAS, 464, 4977
Katsianis, A., Tescari, E., & Wyithe, J. S. B. 2015, MNRAS, 448, 3001
Katsianis, A., Tescari, E., & Wyithe, J. S. B. 2016, PASA, 33, e029
Katsianis, A., Blanc, G., Lagos, C. P., et al. 2017b, MNRAS, 472, 919
Katsianis, A., Zheng, X., Gonzalez, V., et al. 2019, ApJ, 879, 11
Katsianis, A., Gonzalez, V., Barrientos, D., et al. 2020, MNRAS, 492, 5592
Kauffmann, G., Heckman, T. M., White, S. D. M., et al. 2003, MNRAS, 341, 33
Kaviraj, S., Laigle, C., Kimm, T., et al. 2017, MNRAS, 467, 4739
Komatsu, E., Smith, K. M., Dunkley, J., et al. 2011, ApJS, 192, 18
Kroupa, P. 2001, MNRAS, 322, 231
Kurczynski, P., Gawiser, E., Acquaviva, V., et al. 2016, ApJL, 820, L1
Lagos, C. d. P., Tobar, R. J., Robotham, A. S. G., et al. 2018, MNRAS, 481, 3573
Lee, J. C., Gil de Paz, A., Tremonti, C., et al. 2009, ApJ, 706, 599
Lee, N., Sanders, D. B., Casey, C. M., et al. 2013, ApJ, 778, 131
Leja, J., Carnall, A. C., Johnson, B. D., et al. 2019, ApJ, 876, 3
Li, C., & White, S. D. M. 2009, MNRAS, 398, 2177

Lopez, S., Tejos, N., Barrientos, L. F., et al. 2020, MNRAS, 491, 4442
Madau, P., & Dickinson, M. 2014, ARA&A, 52, 415
Meurer, G. R., Heckman, T. M., & Calzetti, D. 1999, ApJ, 521, 64
Monaco, P., Fontanot, F., & Taffoni, G. 2007, MNRAS, 375, 1189
Nelson, D., Pillepich, A., Springel, V., et al. 2018, MNRAS, 475, 624
Nersesian, A., Xilouris, E. M., Bianchi, S., et al. 2019, A&A, 624, A80
Patel, H., Clements, D. L., Vaccari, M., et al. 2013, MNRAS, 428, 291
Pearson, W. J., Wang, L., Hurley, P. D., et al. 2018, A&A, 615, A146
Pillepich, A., Nelson, D., Hernquist, L., et al. 2018a, MNRAS, 475, 648
Pillepich, A., Springel, V., Nelson, D., et al. 2018b, MNRAS, 473, 4077
Robotham, A. S. G., Norberg, P., Driver, S. P., et al. 2011, MNRAS, 416, 2640
Roebuck, E., Sajina, A., Hayward, C. C., et al. 2016, ApJ, 833, 60
Santini, P., Fontana, A., Castellano, M., et al. 2017, ApJ, 847, 76
Schaye, J., Crain, R. A., Bower, R. G., et al. 2015, MNRAS, 446, 521
Schechter, P. 1976, ApJ, 203, 297
Smit, R., Bouwens, R. J., Franx, M., et al. 2012, ApJ, 756, 14
Springel, V. 2010, ARA&A, 48, 391
Springel, V., Pakmor, R., Pillepich, A., et al. 2018, MNRAS, 475, 676
Stoughton, C., Lupton, R. H., Bernardi, M., et al. 2002, AJ, 123, 485
Strauss, M. A., Weinberg, D. H., Lupton, R. H., et al. 2002, AJ, 124, 1810
Tacchella, S., Trenti, M., & Carollo, C. M. 2013, ApJL, 768, L37
Tescari, E., Katsianis, A., Wyithe, J. S. B., et al. 2014, MNRAS, 438, 3490
Tremmel, M., Karcher, M., Governato, F., et al. 2017, MNRAS, 470, 1121
Trčka, A., Baes, M., Camps, P., et al. 2020, MNRAS, 494, 2823
Viaene, S., Baes, M., Tamm, A., et al. 2017, A&A, 599, A64
Vogelsberger, M., Genel, S., Springel, V., et al. 2014, MNRAS, 444, 1518
Weigel, A. K., Schawinski, K., & Bruderer, C. 2016, MNRAS, 459, 2150
Weinberger, R., Springel, V., Hernquist, L., et al. 2017, MNRAS, 465, 3291
Whitaker, K. E., Franx, M., Leja, J., et al. 2014, ApJ, 795, 104
Wuyts, S., Labbé, I., Förster Schreiber, N. M., et al. 2008, ApJ, 682, 985
Xu, H., Zheng, Z., Guo, H., et al. 2016, MNRAS, 460, 3647
Xu, H., Zheng, Z., Guo, H., et al. 2018, MNRAS, 481, 5470
Yang, X., Mo, H. J., van den Bosch, F. C., et al. 2013, ApJ, 770, 115
Yang, X., Mo, H. J., van den Bosch, F. C., et al. 2012, ApJ, 752, 41
York, D. G., Adelman, J., Anderson, John E., J., et al. 2000, AJ, 120, 1579